

1 Thermal behavior study of pristine and modified halloysite nanotubes:
2 a modern kinetic study
3

4 Celia Duce^a, Stefano Vecchio Cipriotti^{b,*}, Lisa Ghezzi^a, Vincenzo Ierardi^c, Maria Rosaria Tinè^a

5 ^aDipartimento di Chimica e Chimica Industriale, Università di Pisa, Via Moruzzi, 56124 Pisa, Italy

6 ^bDipartimento S.B.A.I., Sapienza University of Rome, Via del Castro Laurenziano 7, 00161 Roma, Italy

7 ^cNanoMed Labs, Dipartimento di Fisica, Università di Genova, Via Dodecaneso 33, 16146 Genoa, Italy
8
9

10 **Abstract**

11 Pristine halloysite nanotubes (HNTs) were studied by thermogravimetry (TG) up to 800°C. Etching
12 of alumina from inside the tube (causing a significant increase of tube lumen) was realized by
13 treating the material with an acidic H₂SO₄ solution at 50°C. Both materials were characterized by
14 TG-FTIR techniques and their thermal behaviors were compared with that of kaolinite (KAO). The
15 coupling of TG with FTIR enables to detect the gases evolved during the TG experiments, thus
16 confirming that only pristine HNTs undergo dehydration with the loss of interlayer water molecules
17 at around 245°C, while dehydroxylation occurs in all these materials in close temperature ranges
18 around 500°C. TG runs at five different heating rates (2, 5, 10, 15 and 20 °C min⁻¹) were carried out
19 in the same experimental conditions used for the thermal analysis study with the aim to investigate
20 dehydration and dehydroxylation kinetics using some isoconversional methods, recommended by
21 the ICTAC kinetic committee, and a modulated thermogravimetry heating rate method. Finally, the
22 results of the kinetic analysis were discussed and explained in terms of the strengths of the
23 hydrogen bonds broken during these processes.
24

*Corresponding Author (S. Vecchio Cipriotti)
E-mail Address: stefano.vecchio@uniroma1.it

25 **Introduction**

26 Halloysite is a two-layered aluminosilicate clay with chemical formula $\text{Al}_2\text{Si}_2\text{O}_5(\text{OH})_4 \times n\text{H}_2\text{O}$,
27 consisting of Si-tetrahedral outer sheets joined to Al-octahedral inner sheets by planes of oxygen
28 atoms of tubular shape. Its structure is made up of nano-size tubes having external diameter of 50-
29 80 nm, cylindrical pore (lumen) of 10-15 nm and length of about 1000 nm [1]. Due to this
30 characteristic shape and the presence of less abundant surface hydroxyl groups (with respect to
31 kaolin and montmorillonite) halloysite nanotubes (HNTs) can be dispersed in polymers without the
32 need of exfoliation to form halloysite-polymer composites that are transparent in wide ranges of
33 wavelengths, including near-UV [1-4]. In addition, HNTs is not hazardous for the environment and
34 is available in large amount (thousand of tons) at a very low cost. The outer and inner structure is
35 made up of polar compounds (sheets of $[\text{SiO}_4]$ tetrahedra and sheets of edge-sharing $[\text{AlO}_6]$
36 octahedra), thus providing a good hydrophilicity and therefore a good dispersion in polar polymers,
37 like epoxy, polyethyleneimine, polyamides, polyacrylates, polyvinyl alcohol and biopolymers, like
38 starch, pectin, chitosan, and humic acid [5-10]. Due to their elongated shape and cylindrical lumen,
39 natural HNTs can be loaded with several chemically and biologically active substances [4], like
40 drugs [3,11], proteins [3,12], DNA [13], antibacterials [14], cosmetics [15], thus providing useful
41 bionanocomposite materials for their controlled release for pharmaceutical applications. Sulfuric
42 acid treatments have been provided as an efficient method for enlargement of HNTs lumen diameter
43 with the aim to increase the tube loading capacity. The selective etching of alumina sheets was
44 optimized by tuning time, temperature, and acid concentration; in particular at high level of etching
45 (above 30-40% of dealumination) halloysite gradually loses its tubular morphology [16].

46 Nowadays it is not clear how HNTs are formed in nature. According to some authors, kaolinite
47 (KAO), with a layer structure consisting of superimposed silicon tetrahedral sheets and aluminum
48 octahedral sheets, is the main mineral phase of kaolin having the same chemical formula of
49 halloysite. It is demonstrated that KAO may roll leading to the formation of HNTs [17]. KAO is an
50 important material used in several industrial processes like food-processing industry, oil shale

51 processing, ceramic industry, as a pozzolanic material or as a filling agent, and for its use it is pre-
52 heated at high temperature (from 450 to 700°C) until it is transformed to metakaolin via
53 dehydroxylation [18]. Dehydroxylation, elimination of water from hydroxyl groups, is an important
54 thermal dissociation reaction among those occurring in the kaolinite group minerals and in natural
55 or synthesized silicate materials [19]. Non-isothermal kinetics of this process, which occurs at
56 temperature quite higher than dehydration due to the presence of stronger hydrogen bonds between
57 the OH groups, was extensively studied for different type of KAOs [18,20-24], but little is known
58 about the same process occurring in HNTs where early papers used questionable methods under
59 isothermal conditions [25,26].

60 Some authors adopted in their studies [21b-c,24] kinetic approaches (in particular, model-fitting
61 methods) that the ICTAC kinetics committee demonstrated to provide unreliable results [27].
62 Furthermore, Liu and co-worked recently applied an early method to study dehydroxylation of
63 synthetic Al-goethite, providing unreasonable low activation energies between 3 and 7 kJ mol⁻¹
64 [28]. Therefore, a first aim of this study is to investigate the thermal behavior of pristine and
65 modified via lumen enlargement HNTs and to compare it with that of KAO. A second aim is to
66 provide an exhaustive description of kinetic analysis of both dehydration (for HNTs only) and
67 dehydroxylation processes occurring in pristine and modified HNTs (treated at 50°C with sulfuric
68 acid), with a view to correlate the results obtained with the different structures of these materials. In
69 particular the coupling of thermogravimetry (TG) with FTIR enabled to completely characterize the
70 thermal degradation of HNTs (both pristine and etched) whereas TG experiments performed at
71 different heating rates were used for the kinetic study. The data so obtained were analysed by
72 several isoconversional methods and compared with those obtained by modulated
73 thermogravimetry.

74

75

76 **Theoretical background**

77 The kinetic description of thermally stimulated processes occurring in materials in the condensed
 78 phase is rather more complex than that for homogeneous reactions. The first difficulty arises from
 79 the definition of the function describing the progress of the reaction against time (under isothermal
 80 condition) or temperature (under the most commonly used non-isothermal condition with constant
 81 heating rate $\beta=dT/dt$). The so-called degree of conversion α , which is 0 at the initial temperature T_i
 82 and 1 at the final temperature T_f of each step, is defined as $\alpha=(m_i-m_T)/(m_i-m_f)$, where m_i , m_f and m_T
 83 are the sample masses at the corresponding T_i , T_f and T according to thermogravimetric (TG) data.
 84 The explicit dependence of the reaction rate by both the absolute temperature and the extent of
 85 conversion α , strictly valid under the assumption of a of a single-step process, is expressed by the
 86 following equation

$$\frac{d\alpha}{dt} = k(T)f(\alpha) \quad (1)$$

87 where $k(T)$ usually represents the rate constant, commonly used in the form of the Arrhenius
 88 equation that enable to re-write Eq. (1) in the following form

$$\frac{d\alpha}{dt} = Ae^{-E/RT}f(\alpha)$$

91 (2)

92 where A is the pre-exponential factor, E is the activation energy and $f(\alpha)$ is a function called
 93 reaction model [29,30].

94 For experiments carried out under modulated heating rate conditions using an oscillatory
 95 temperature program (temperature increases “smoothly varying temperature sine wave” [31]), the
 96 ratio between the reaction rates expressed in Eq. (2) and calculated at the peak and valley of the
 97 sinusoidal wave form (α_p and α_v), can be derived as follows:

$$\frac{d\alpha_p/dt}{d\alpha_v/dt} = \frac{e^{-E/RT_p}f(\alpha_p)}{e^{-E/RT_v}f(\alpha_v)} \quad (3)$$

98 where the $\ln((\alpha_p/\alpha_v))$ signal is obtained using a Fourier transformation. Under constant conversion
 100 condition (or at least for small variation between adjacent peaks and valley) the ratio $f(\alpha_p)/f(\alpha_v)$

101 approaches unity, being $f(\alpha_p) \approx f(\alpha_v)$. Taking the logarithm of both sides of Eq. (3) and solving for E
 102 yields:

$$103 \quad E = \frac{RT_p T_v \ln(d\alpha_p/d\alpha_v)}{T_p - T_v} \quad (4)$$

104 In any oscillatory temperature program, T_p and T_v are defined as $T_p = \langle T \rangle + A$ and $T_v = \langle T \rangle - A$,
 105 where $\langle T \rangle$ is the average temperature, A is the temperature amplitude, while $T_p - T_v = 2A$. Eq. (4)
 106 can be further simplified by introducing a new parameter L , which is set equal to the peak-to-peak
 107 amplitude of the $\ln(d\alpha)$ signal ($L = \ln d\alpha_p - \ln d\alpha_v$). Once the values have been replaced in Eq. (4),
 108 it assumes the following more simple form:

$$109 \quad E = \frac{R(T^2 - A^2)L}{2A} \quad (5)$$

110 It is worth noting that a kinetic method based on Eq. (5) is among those called “model-free”, as its
 111 computations do not depend on the knowledge of the choice of a proper model function $f(\alpha)$.

112 On the other hand, approaches based on multiple heating rate (or temperature) programs are highly
 113 recommended by the ICTAC Kinetic Committee [32]. The time dependency of reaction rate $d\alpha/dt$
 114 is then replaced by its corresponding temperature dependency $d\alpha/dT = \beta^{-1} d\alpha/dt$ reaction rate,
 115 giving Eq. (6):

$$116 \quad \frac{d\alpha}{dT} = \left(\frac{A}{\beta}\right) e^{-E/RT} f(\alpha)$$

117 (6)

118 Separation of variables in Eq. (6) yields:

$$119 \quad \frac{d\alpha}{f(\alpha)} = \left(\frac{A}{\beta}\right) e^{-E/RT} dT$$

120 (7)

121 The integrals of both the left- and right-hand side of Eq. (7) gives:

$$122 \quad \int_0^\alpha \frac{d\alpha}{f(\alpha)} = g(\alpha) = \left(\frac{A}{\beta}\right) \int_0^T e^{-E/RT} dT$$

123 (8).

124 The temperature integral in Eq. (8) has no exact analytical but approximate solutions that give rise

125 to some of the most commonly isoconversional methods, whose equations for each fixed extent of
 126 conversion α have the following general form:

$$127 \quad \ln\left(\frac{\beta}{T^B}\right)_\alpha = Const - C\left(\frac{E}{R}\right)\left(\frac{1}{T}\right)_\alpha \quad (9)$$

128 where B and C are adjustable parameters, whose values depend on the approximation made. In
 129 particular, for the Ozawa-Flynn-Wall (OFW) method [33,34], based on the Doyle's approximation
 130 [35], $B=0$ and $C=1.052$. More accurate results can be obtained using the Kissinger-Akahira-Sunose
 131 (KAS) method [36], where $B=2$ and $C=1$ or the Starink (STA) method [37] ($B=1.92$ and $C=1.008$).
 132 Each value of activation energy at each given extent of conversion is calculated from the slope of
 133 the regression line obtained by plotting the left-hand side of Eq. (9) against the reciprocal
 134 temperature $(T^{-1})_\alpha$. Isoconversional methods, along with the invariant kinetic parameters [38,39]
 135 and the constant rate thermal analysis (CRTA) [40,41], are recognized to be among those who
 136 usually give reliable results and relevant books, review and papers [27,29,42,43] deal with the
 137 advantage of their use. These methods are based on the assumption that the reaction rate at constant
 138 degree of conversion is only a function of temperature. Vyazovkin developed a method (VYA) that
 139 gives results with a better accuracy by numerical integration of the right-hand side of Eq. (5) [44-
 140 46] by minimizing the following function:

$$141 \quad \phi(E_\alpha) = \sum_{i=1}^n \sum_{j \neq i}^n \frac{J[E_\alpha, T_i(t_\alpha)]}{J[E_\alpha, T_j(t_\alpha)]} \quad (10)$$

142 where $J[E_\alpha, T(t_\alpha)] = \int_0^{T_\alpha} \exp[-E_\alpha/RT(t)]dT$ is solved numerically and minimization is made for each
 143 value of α with the aim to obtain a conversion dependency of activation energy. The reaction model
 144 and the α -dependence of pre-exponential factor ($\ln A_\alpha$) can be accurately determined only in the
 145 case of processes that follow approximately a single-step kinetics, for which it can be expected that
 146 activation energy does not varies appreciably over the entire range of the extent of conversion α by
 147 combining the results of isoconversional (model-free) and model-fitting methods [47]. By applying
 148 a model-fitting method (Coats-Redfern [48] in this study) a pair of Arrhenius parameters can be

149 obtained for each reaction model using a single-heating rate experiment. Wide ranges of values are
150 found for both parameters when all the reaction models are considered, but a strong linear
151 correlation denoted as compensation effect is found between them in the following form:

$$152 \quad \ln A_i = aE_i + b \quad (11)$$

153 where the subscript i refers to each of all the reaction model. Once a and b parameters have been
154 determined at each heating rate using a linear regression procedure, these values were replaced in
155 Eq. (11) by their mean values $\langle a \rangle$ and $\langle b \rangle$ while the E_i values were replaced by the
156 isoconversional values of E_α to determine the corresponding values of $\ln A_\alpha$ for each given value of
157 α [47].

158

159

160 **Experimental**

161 **Materials**

162 Kaolinite and pristine halloysite nanotubes were purchased from Sigma Aldrich and used without
163 further purification. The procedure followed for the HNT lumen etching was similar to that reported
164 in literature [16]. A suspension of halloysite was obtained by dispersing 5 g of Halloysite in 300 ml
165 of a 2 mol l⁻¹ H₂SO₄ solution. The suspension was magnetically stirred for 48 hours on a hot plate
166 at the controlled temperature of 50 °C. The processed halloysite was then washed with distilled
167 water until the pH of the supernatant from the washing stage was in the range 6-7, similar to that of
168 pure halloysite suspension. The sample was dried in an oven at 50°C and then characterized by TG.

169

170 **Instruments**

171 Samples were analyzed through scanning electron microscopy (SEM) and scanning transmission
172 electron microscopy (STEM). Images were collected using an Ultra High Resolution Field
173 Emission Scanning Electron Microscopy (UHR-FE-SEM) by Zeiss equipped with a STEM. In order

174 to collect SEM images, powder of pristine and etched HNTs have been deposited onto a substrate of
175 copper. Instead the STEM samples were prepared using as substrate a TEM grid.

176 All the TG experiments were performed using a TA Instruments Q5000IR thermogravimetric
177 instrument equipped with an FTIR(Agilent Technologies) Cary 640 spectrophotometer for
178 Evolved Gas Analysis (EGA). The Q5000IR thermogravimetric analyzer has the optional capability
179 to work in modulated mode (modulated thermogravimetry, MTG). TG measurements were
180 performed in this study with both dynamic conventional (constant heating rate) and modulated
181 temperature programs. Both types of experiments were carried out from 40 to 800 °C using Pt
182 crucibles under a stream of air of 25 ml min⁻¹. In conventional TG, samples were heated at five
183 different heating rates (2, 5, 10, 15, 20 °C min⁻¹) to process TG data for kinetic computations. In
184 MTGA experiments samples were heated at a heating rate of 2° C min⁻¹ with a temperature
185 modulation amplitude of ± 5°C and a period of 200 s. The MTG curves were analyzed using the TA
186 Universal Analysis 2000 software TG-FTIR measurements were performed at a rate of 20°C min⁻¹,
187 from 40°C to 800°C under air flow (70 ml min⁻¹), from 600 to 3000 cm⁻¹ with a 4 cm⁻¹ width slit.
188 To reduce the background absorption from water and carbon dioxide in the atmosphere, the optical
189 banch was purged with nitrogen. In addition, a background spectrum was taken before each analysis
190 in ordet to zero the signal in the gas cell and to eliminate the contribution due to the amount of
191 ambient water and carbon dioxide. The amount of sample in each TG and TG.FTIR measurement
192 varied between 4 and 8 mg .

193

194

195 **Results and discussion**

196 Treatments with sulfuric acid have been provided as an efficient method for enlargement of HNTs
197 lumen diameter with the aim to increase the tube loading capacity [16]. The increase of the HNTs
198 lumen, after acidic treatment, is clearly evident in Fig. 1, where it is possible to see some examples
199 of SEM and STEM images of pristine and etched HNTs. STEM combines the principles of

200 transmission electron microscopy and scanning electron microscopy. Its primary advantage over
201 conventional SEM imaging is the improvement in spatial resolution with consequently better
202 imaging resolution.

203 Fig. 1a-b shows the STEM images of pristine and etched HNTs, respectively. The arrows and the
204 dashed lines highlight the size of the HNT lumen, which, in the case of pristine HNTs, is 15-20 nm;
205 while in etched HNTs, because of the etching process, increases up to 30-40 nm. The enlargement
206 of lumen size is further supported by SEM images (Fig. 1c-d). As could be expected the images of
207 etched HNTs (Fig. 1b,d) show changes in halloysite morphology. Indeed, although the rodlike
208 structure was preserved, the etched tubes present broken points and the halloysite walls appear more
209 friable and porous.

210 The TG/DTG curves of pristine HNTs, etched HNTs and KAO are given in Fig. 2. Relevant data
211 taken from these measurements (peak DTG temperatures and mass loss percentages) of each step
212 are shown in Table 1. The thermal behavior of HNTs and etched HNTs showed remarkable
213 differences. In particular, pristine HNTs undergo four steps of mass loss, the first of which at
214 $T_p=37.5$ °C (mass loss 2.3%) is due to water physically adsorbed to the surface, while the second, in
215 the range 200-285 °C (mass loss 3.3%), is ascribed to the release of interlayer water molecules
216 bound by hydrogen bonds. The third step is due to dehydroxylation (condensation of hydroxyl
217 groups of aluminum inner sheets) around 470°C (mass loss 11.4%), while at 744°C the mass loss of
218 1.7% is ascribed to the release of SO₂ due to the thermal decomposition of sulfides (as impurity) or
219 alunite, according to what it was recently reported in literature [20,49], even for kaolin [50]. The
220 hypothesis that the mass losses below 500°C could be exclusively due to water release, is confirmed
221 by FTIR analysis. The gas evolved at the fixed temperatures of 37.5, 245 and 468 °C present the
222 same spectrum (see Fig. 3a) showing the narrow bands at 4000-3500 and 2000-1300 cm⁻¹ typical of
223 the spectrum of water [51]. On subsequent heating, the spectrum recorded at 750°C (Fig. 3b) shows
224 the characteristic bands of SO₂ impurities (1390, 1338 and 1180 cm⁻¹) [51, 52].

225 By contrast, etched HNTs did not show the loss of interlayer water around 245°C, thus
226 demonstrating that the acidic etching at 50°C, responsible for the enlargement of HNTs lumen [16],
227 caused the elimination of the interlayer water. The water loss attributed to dehydroxylation takes
228 place at temperature slightly higher (T_p at 479°C instead of 468 °C), and with a lower mass loss
229 (6.0% instead of 11.4%) than in pristine HNTs. As expected, around 730°C the loss of SO₂ is
230 confirmed also in etched HNTs. No dehydration is shown for KAO that is stable up to 330 °C in
231 agreement with the results reported in [53], while other authors found in the temperature range up to
232 150°C a slight mass loss due to dehydration [20,21c]. Dehydroxylation occurs in a single step in the
233 wide temperature range between 400 and 700°C in agreement with literature findings
234 [18,20,21c,22,50].

235 Eqs. 10 and 11 were considered to apply the four isoconversional methods denoted as OFW, KAS,
236 STA and VYA to analyze the kinetics of dehydration in HNTs by processing TG data between 200
237 and 280°C (Fig. 2), and dehydroxylation in HNTs, etched HNTs and KAO in the temperature range
238 close to 470-500°C. The results of kinetic analysis regarding dehydration and dehydroxylation,
239 reported as the usual conversion dependency of activation energy, are summarized in Figs. 4 and 5,
240 respectively. Interpretation of these results should be made in terms of the energy barrier to be
241 overcome by water molecules to proceed with dehydration or dehydroxylation. Application of
242 OFW, KAS and STA methods to dehydration of HNTs seems to fail due to the significant change in
243 E_α values preventing the use of Eq. (7) that implies separation of variables, and is rigorously valid
244 only if neither the model function $f(\alpha)$ depends on temperature nor activation energy E_α on the
245 degree of conversion. Furthermore, these results indicate a multi-step nature of the process
246 investigated. However, the results of the VYA method, which can be applied even in the case of
247 remarkable variation of E_α values, are in close agreement with those determined with the previous
248 cited methods (in particular in the range $0.55 < \alpha < 0.95$, where E_α drops from 170 to 38 kJ mol⁻¹). It
249 is worth noting that these values are markedly higher than the molar vaporization enthalpy of water

250 ($\approx 44 \text{ kJ mol}^{-1}$). On the other hand, the temperature range for the occurrence of this process (200-
251 280°C) is remarkably higher than that of pure water. At this regard, water vaporization kinetics
252 from bulk and from clays was recently investigated [54] and average values ranging from 43.8 to
253 56.2 kJ mol^{-1} were obtained for the former and the latter materials, respectively, because of the low
254 temperature range of the occurrence of this process (from -20 to 90°C).

255 However, at the beginning of dehydration process of HNTs ($\alpha < 0.30$) the E_α values obtained by the
256 VYA method increase from 180 to 200 kJ mol^{-1} and then decreases to about 175 kJ mol^{-1} . Actually,
257 these change of E_α values are not so high (slightly higher than the associated uncertainties) even if
258 they cannot be neglected. In general, increasing and decreasing trends of E_α values should be
259 interpreted in terms of the increase or decrease of the energy barrier for the occurrence of the
260 process examined. A decrease followed by an increase of water molecular mobility occurring
261 during heating can be probably the main factor that generated those variations of E_α values. On the
262 other hand, water molecular mobility is particularly affected by the rupture of weaker hydrogen
263 bonds within the $[\text{AlO}_6]$ octahedra inner sheets. Constant E_α values ($\approx 171 \text{ kJ mol}^{-1}$) were found in
264 the range $0.30 \leq \alpha < 0.60$, followed by a significant decrease to the values usually considered for free
265 vaporization of pure water ($40\text{-}45 \text{ kJ mol}^{-1}$). The decreasing trend of E_α values at the end of the
266 process can be explained by the fact that the water molecular mobility increases up to values
267 comparable to those found in bulk pure water. The results obtained with MTG, which adopted a
268 differential isoconversional approach with respect to the integral one offered by OFW, KAS and
269 STA, is completely in disagreement with those of all other methods considered at the beginning
270 ($\alpha < 0.30$) and at the completion ($\alpha > 0.80$) of the process. A reasonable explanation of these large
271 deviations can be ascribed to the approximation made in Eqs. (3-4) to consider $f(\alpha_p) \approx f(\alpha_v)$, which is
272 reasonably valid in most of the conversion ranges. However, this approximation is inapplicable for
273 n-th order models when the values of α approach unity and for the autocatalytic model function
274 when α approaches either zero or unity (as in the case of dehydration of HNTs examined in this

275 study) [31]. Slight higher values of E (of about 40 kJ mol^{-1}) are also found in the range
276 $0.30 \leq \alpha < 0.80$, which are practically constant, similarly to what it is observed using all the other
277 methods.

278 In Fig. 5a substantial agreement is found among the isoconversional dependencies of E_α values
279 related to dehydroxylation determined using the five methods and the slight differences between the
280 results of the first three integral approaches (OFW, KAS and STA) and those of VYA and MTG are
281 limited to small ranges of α values. Large deviations of E values calculated using the MTG method
282 when α approaches zero and unity is attributed (as in the case of dehydration of HNTs) to the
283 failure of the approximation $f(\alpha_p) \approx f(\alpha_v)$ when a process (as probably in this case) can be described
284 by a autocatalytic model function [31]. Dehydroxylation in HNTs showed a trend similar to that of
285 dehydration in the range up to $\alpha=0.40$, followed by practical constant E_α values (around $190\text{-}200 \text{ kJ}$
286 mol^{-1}), in close agreement (within a usual estimated uncertainty around $5\text{-}7\%$) with the single value
287 found in literature ($\approx 185 \text{ kJ mol}^{-1}$) [26]. As expected, quite higher E_α values are shown in the case
288 of etched HNTs (Fig. 5b) and good agreements are found among the E_α values determined with the
289 five methods applied (except in the case of the MTG method for $\alpha \approx 0$ and $\alpha \approx 1$). An increasing trend
290 of E_α values can be attributed to a decreasing trend in molecular mobility of water (obtained by
291 condensation of hydroxyl groups) during the course of the process, probably caused by the etching
292 of $[\text{AlO}_6]$ inner sheets. At a first sight, dehydroxylation of KAO (Fig. 5c) seems to be described in
293 a more simple way, with superimposable and practically constant values of E_α determined by the
294 five methods (around 220 kJ mol^{-1}) for $\alpha < 0.6$. A good agreement (at least in the range $\alpha < 0.70$) is
295 found also with literature data on KAO [21c] and with the values determined for etched HNTs.
296 Remarkable deviation of the E_α values determined with the MTG method is shown in the range
297 $\alpha > 0.8$, ascribed to the above-cited failure of the approximation $f(\alpha_p) \approx f(\alpha_v)$, thus suggesting in this
298 case that the mechanism of dehydroxylation of KAO can be reasonably described using n-th order
299 models [31].

300 These findings, along with the comparison of their thermal behavior, suggest that the lumen
301 enlargement caused by the acidic etching of the inner sheets of aluminum oxide provides a material
302 even more similar to KAO than pristine HNTs.

303

304

305 **Conclusions**

306 Coupling of TG and FTIR techniques demonstrated in this study to be a useful tool to investigate
307 the thermal behavior of both pristine and etched HNTs. The acidic etching of the $[AlO_6]$ octahedra
308 inner sheets of pristine HNTs is a common procedure used to enlarge the cylindrical lumens in
309 order to load HNTs with suitable amounts of chemically and biologically active substances. SEM
310 and STEM techniques used in this study confirmed to be able in providing images proving
311 indubitably that the etching of HNTs produced changes in halloysite morphology. Although the
312 rodlike structure was preserved, the etched tubes presented broken points and the halloysite walls
313 appeared more friable and porous. These structural changes are responsible of relevant changes in
314 the thermal behavior of HNTs (*i.e.*, lost of layered water molecules) that appears more similar to
315 kaolinite (tested only for comparison purpose) than to precursor. A modern kinetic analysis of both
316 dehydration and dehydroxylation processes was performed in accordance with recent ICTAC
317 recommendations. Different differential (MTG) and integral (OFW, KAS, STA and VYA)
318 isoconversional methods confirmed the complex multi-step nature of both processes, evidenced by
319 the non-negligible variation of E_α with increasing the degree of conversion. Increasing and
320 decreasing trends of E_α values were interpreted in terms of increase and decrease of the molecular
321 mobility of water hypothesized during the occurrence of these processes.

322

323

324 **Acknowledgements**

325 The authors acknowledge the financial support from FIRB 2012, *Clay nanotubes for designing eco-*
326 *compatible smart materials*, funded by the Italian Ministry of University and Research (Project
327 No.RBFR12ETL5) and Dr. Giuseppe Lazzara and Prof. Peter Simon for helpful discussions.

328 **References**

329

- 330 1. Du M, Guo B, Jia D. Newly emerging applications of halloysite nanotubes: a review. *Polym.*
331 *Int.* 2010;59:574-95.
- 332 2. Price R, Gaber B, Lvov Y. In vitro release characteristics of tetracycline, khellin and
333 nicotinamide adenine dinucleotide from halloysite; a cylindrical mineral for delivery of
334 biologically active agents. *J. Microencapsul.* 2001;18:713-23.
- 335 3. Abdullayev E, Lvov Y. Clay nanotubes for corrosion inhibitor encapsulation: release control
336 with end stoppers. *J. Mater. Chem.* 2010;20:6681-7.
- 337 4. Abdullayev E, Lvov Y. Clay nanotubes for controlled release of protective agents – a
338 review. *J. Nanosci. Nanotechnol.* 2011;11:10007-26.
- 339 5. Liu M, Guo B, Du M, Cai X, Jia D. Properties of halloysite nanotube-epoxy resin hybrids
340 and the interfacial reactions in the systems. *Nanotech.* 2007;18: 455703/1-9.
- 341 6. Abdullayev E, Lvov Y. Halloysite clay nanotubes as a ceramic “skeleton” for functional
342 biopolymer composites with sustained drug release. *J. Mater. Chem. B* 2013;1:2894-903.
- 343 7. Lvov Y, Price R, Gaber B. Thin film nanofabrication via layer-by-layer adsorption of tubule
344 halloysite, spherical silica, proteins and polycations. *Coll. Surf. A* 2002;198-200:375-82.
- 345 8. Liu M, Guo B, Du M, Jia D. Drying induced aggregation of halloysite nanotubes in
346 polyvinyl alcohol/halloysite nanotubes solution and its effects on properties of composite
347 films. *Appl. Phys. A* 2007;88:391-5.
- 348 9. Wei W, Abdullayev E, Hollister A, Mills D, Lvov Y. Clay nanotube/poly(methyl
349 methacrylate) bone cement composite with sustained antibiotic release. *Macromol. Mater.*
350 *Eng.* 2012;297:645–53.
- 351 10. Cavallaro G, Lazzara G, Milioto S. Dispersions of nanoclays of different shapes into
352 aqueous and solid biopolymeric matrices. Extended physico-chemical study. *Langmuir*
353 2011;27:1158–63.
- 354 11. Veerabadran N, Price R, Lvov Y. Clay nanotubes for encapsulation and sustained release of
355 drugs. *NANO* 2007;2:215–22.
- 356 12. Shchukin D, Price R, Lvov Y. Biomimetic synthesis of vaterite in the interior of clay
357 nanotubules. *Small* 2005;1:510–3.
- 358 13. Shamsi MH, Geckeler KE. The first biopolymer-wrapped non carbon nanotubes. *e-Nanotech*
359 2008;19:1–5.
- 360 14. Joshi A, Abdullayev E, Vasiliev A, Volkova O, Lvov Y. Interfacial modification of clay
361 nanotubes for the sustained release of corrosion inhibitors. *Langmuir* 2013;29:7439–48.

- 362 15. Suh Y, Kil D, Chung K, Abdullayev E, Lvov Y, Mongayt D. Natural nanocontainer for the
363 controlled delivery of glycerol as a moisturizing agent. *Journal of Nanoscience and*
364 *Nanotechnology* 2011;11:661–5.
- 365 16. Abdullayev E, Joshi A, Wei W, Zhao Y, Lvov Y. Enlargement of Halloysite Clay Nanotube
366 Lumen by Selective Etching of Aluminium Oxide. *ACSNANO* 2012;6(8):72167226.
- 367 17. Singh B. Why does halloysite roll? – a new model. *Clays and Clay Minerals* 1996;44:191–6.
- 368 18. Gasparini E, Tarantino S.C., Ghigna P, Riccardi MP, Cedillo-González EI, Siligardi C,
369 Zema M. Thermal dehydroxylation of kaolinite under isothermal conditions. *Appl Clay Sci.*
370 2013;80-81:417–25.
- 371 19. Vecchio Cipriotti S, Catauro M. Synthesis, thermal behavior and FTIR study of some
372 calcium silicate gel-glasses of general formula $x\text{CaO} \cdot (1-x)\text{SiO}_2$. Kinetic analysis of their
373 dehydration and dehydroxylation processes. Submitted to *Thermochimica Acta*, 2014.
- 374 20. Cheng H, Yang J, Liu Q, Frost RL. Thermogravimetric analysis–mass spectrometry (TG–
375 MS) of selected Chinese kaolinites. *Thermochim. Acta* 2010;507-508:106–14.
- 376 21. Ptáček P, Soukal F, Opravil T, Havlica J, Brandstetr J. The kinetic analysis of the thermal
377 decomposition of kaolinite by DTG technique. *Powder Technol.* 2011;208:20-5; Ptáček P,
378 Soukal F, Opravil T, Nosková M, Havlica J. The non-isothermal kinetics analysis of the
379 thermal decomposition of kaolinite by effluent gas analysis technique, *Powder Technol.*
380 2010;203:272–6; Ptáček P, Kubatova D, Havlica J, Brandstetr J, Soukal F. Isothermal kinetic
381 analysis of the thermal decomposition of kaolinite: the thermogravimetric study.
382 *Thermochim Acta* 2010;501:24–9.
- 383 22. L’vov BV, Ugolkov VL. Kinetics and mechanism of dehydration of kaolinite, muscovite and
384 talc analyzed thermogravimetrically by the third-law method. *J Therm Anal Calorim.*
385 2005;82:15–22.
- 386 23. González Sánchez F, Van Loon LR, Ginni T, Jakob A, Glaus MA, Diamond LW. Self-
387 diffusion of water and its dependence on temperature and ionic strength in highly compacted
388 montmorillonite, illite and kaolinite. *Appl Geochem.* 2008;23:3840–51.
- 389 24. Klevtsov DP, Logvinenko VA, Zolotovskii BP, Krivoruchko OP, Buyanov RA. Kinetics of
390 kaolinite dehydration and its dependence on mechanochemical activation. *J Therm Anal.*
391 1988;33:531–5.
- 392 25. Adhikaria M, Majumdara MK, Pati AK. Thermal Decomposition of Vermiculites: Kinetics
393 of Dehydration and Dehydroxylation Processes. *Trans Ind Ceram Soc.* 1983;42(5)124–7.
- 394 26. Murray P, White J. Kinetics of clay dehydration. *Clay Miner.* 1955;2:255–64.
- 395 27. Vyazovkin S, Burnham AK, Criado JM, Pérez-Maqueda LA, Popescu C, Sbirrazzuoli N.

- 396 ICTAC Kinetic Committee recommendations for performing kinetic computations on
397 thermal analysis data. *Thermochim Acta* 2011;520:1–19.
- 398 28. Liu H, Chen T, Xie Q, Zou X, Qing C, Frost RL. Kinetic study of goethite dehydration and
399 the effect of aluminium substitution on the dehydrate. *Thermochim Acta* 2012;545:20–5.
- 400 29. Brown ME, Dollimore D, Galwey AK. *Reactions in the Solid State. Comprehensive*
401 *Chemical Kinetics, Vol. 22, Amsterdam; Elsevier; 1980.*
- 402 30. Sestak J. *Thermophysical Properties of Solids. Comprehensive Analytical Chemistry, Vol.*
403 *12D, Amsterdam; Elsevier; 1984.*
- 404 31. Blaine RL, Hahn BK. Obtaining kinetic parameters by modulated thermogravimetry. *J*
405 *Therm Anal.* 1998;54:695–704.
- 406 32. Brown ME, Maciejewski M, Vyazovkin S, Nomen R, Sempere J, Burnham A, Opfermann J,
407 Strey R, Anderson HL, Kemmler A, Keuleers R, Janssens J, Desseyn HO, Li CR, Tang TB,
408 Roduit B, Malek J, Mitsuhashi T. Computational aspects of kinetic analysis Part A: The
409 ICTAC kinetics project-data, methods and results. *Thermochim Acta* 2000;355:125–43.
- 410 33. Flynn JH, Wall LA. A quick direct method for the determination of activation energy from
411 thermogravimetric data. *J Polym Sci B: Polym Lett.* 1966;4(5):323–8.
- 412 34. Ozawa T. A new method of analyzing thermogravimetric data. *Bull Chem Soc Jpn.*
413 1965;38:1881–6.
- 414 35. Doyle CD. Estimating isothermal life from thermogravimetric data. *J Appl Polym Sci.*
415 1962;6(24):639–42.
- 416 36. Akahira T, Sunose T. Paper No. 246, 1969 Research Report, Trans. Joint Convention of
417 Four Electrical Institutes. *Chiba Inst Technol (Sci. Technol.)* 1971;16:22–31.
- 418 37. Starink MJ. The determination of activation energy from linear heating rate experiments: a
419 comparison of the accuracy of isoconversion methods, *Thermochim Acta* 2003;404:163–76.
- 420 38. Lesnikovich AI, Levchik SV. Isoparametric kinetic relations for chemical transformations in
421 condensed substances (Analytical survey). II. Reactions involving the participation of solid
422 substances. *J Therm Anal.* 1985;30:677–702.
- 423 39. Lesnikovich AI, Levchik SV. A method of finding invariant values of kinetic parameters, *J.*
424 *Therm. Anal.* 1983;27:89–93.
- 425 40. Pérez-Maqueda LA, Criado JM, Sánchez-Jiménez PE, Perejón A. Kinetic studies in solid
426 state reactions by sample-controlled methods and advanced analysis procedures. *J Therm*
427 *Anal Calorim.* 2013;113:1447–53.

- 428 41. Pérez-Maqueda LA, Criado JM, Gotor FJ, Málek J. Advantages of Combined Kinetic
429 Analysis of Experimental Data Obtained under Any Heating Profile. *J Phys Chem A*
430 2002;106:2862–8.
- 431 42. Vyazovkin S, Wight CA. Kinetics in solids. *Annu Rev Phys Chem.* 1997;48:125–49.
- 432 43. Simon P. Isoconversional methods. Fundamentals, meaning and application. *J Therm Anal*
433 *Calorim.* 2004;74:123–32.
- 434 44. Vyazovkin S. Evaluation of the activation energy of thermally stimulated solid-state
435 reactions under an arbitrary variation of the temperature. *J Comput Chem.* 1997;18:393–402.
- 436 45. Vyazovkin S. Modification of the integral isoconversional method to account for variation in
437 the activation energy. *J Comput Chem.* 2001;22:178–183.
- 438 46. Vyazovkin S, Dollimore D. Linear and non linear procedures in isoconversional
439 computations of the activation energy of thermally induced reactions in solids, *J Chem Inf*
440 *Comp Sci.* 1996;36:42–5.
- 441 47. Budrugaec P, Segal E. Thermal analysis in the evaluation of thermal lifetime of solid
442 polymeric materials. *Thermochim Acta* 1992;211:131–6.
- 443 48. Coats AW, Redfern JP. Kinetic parameters for thermogravimetric data. *Nature* 1964;201:68–
444 9.
- 445 49. Garcia FJ, Rodríguez SG, Kalytta A, Reller A. Study of Natural Halloysite from the Dragon
446 Mine, Utah (USA). *Z Anorg Allg Chem.* 2009;635(4 - 5):790–5.
- 447 50. Badogiannis E, Kakali G, Tsivilis S. Metakaolin as supplementary cementitious material.
448 Optimization of kaolin to metakaolin conversion. *J Therm Anal Calorim.* 2005;81:457–62.
- 449 51. NIST Chemistry WebBook Standard Reference Database, <http://webbook.nist.gov/chemistry>
- 450 52. da Silveira Petrucci JF, Fortes PR, Kokoric V, Wilk A, Raimundo Jr. IM, Cardoso AA,
451 Mizaikoff B. Monitoring of hydrogen sulfide via substrate-integrated hollow waveguide mid-
452 infrared sensors in real-time. *Analyst* 2014;139:198–203.
- 453 53. Heide K, Foldvari M. High temperature mass spectrometric gas-release studies of kaolinite
454 $\text{Al}_2[\text{Si}_2\text{O}_5(\text{OH})_4]$ decomposition. *Thermochim Acta* 2006;446:106–12.
- 455 54. Prado JR, Vyazovkin S. Activation energies of water vaporization from the bulk and from
456 laponite, montmorillonite, and chitosan powders. *Thermochim Acta* 2011;524:197–201.

457 **Table 1** Comparison of experimental DTG peak temperatures T_p and
 458 mass loss percentages for all the steps evaluated from the TG curves
 459 performed at $10\text{ }^\circ\text{C min}^{-1}$ under a stream of air for all the
 460 investigated materials

Process	$T_p / ^\circ\text{C}$			Mass Loss/%		
	HNTs	etched HNTs	KAO	HNTs	etched HNTs	KAO
Dehydration (step 1)	37.5	39.5	n.d.	2.3	4.2	n.d.
Dehydration (step 2)	245	n.d.	n.d.	3.3	n.d.	n.d.
Dehydroxylation	468	479	503	11.4	6.0	11.0
Thermal Decomposition (loss of sulfide)	744	730	n.d.	1.7	3.4	n.d.

461 n.d. = not detected

462

463

464 Captions of the figures

465 **Fig. 1** *a* STEM image of pristine HNTs, *b* STEM image of etched HNTs, *c* SEM image of pristine
 466 HNTs, *d* SEM image of etched HNTs.

467

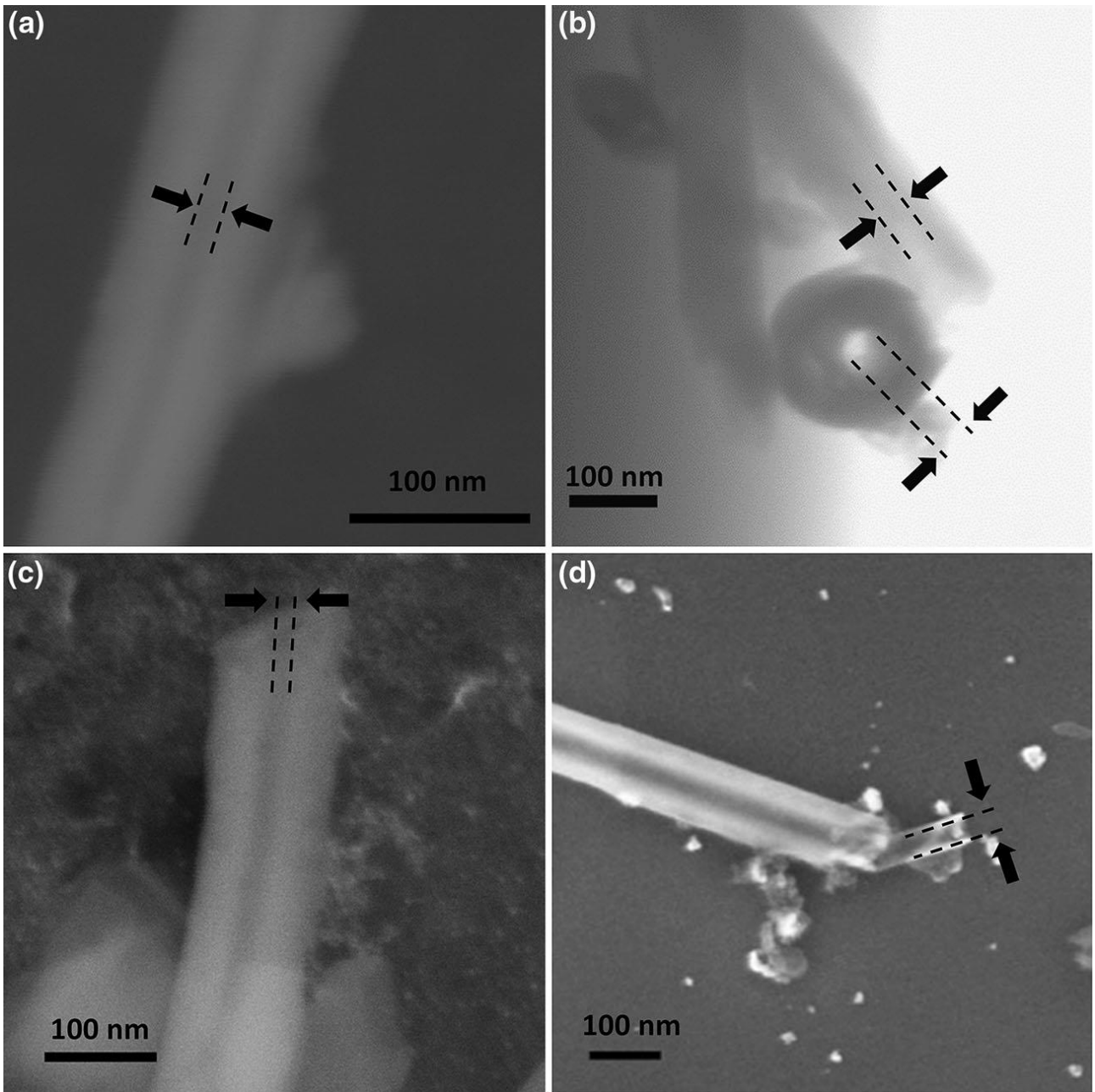
468 **Fig. 2** *a* TG and *b* DTG curves of the materials investigated under a stream of air at $10\text{ }^\circ\text{C min}^{-1}$.

469 **Fig. 3** FTIR spectra of gases evolved during the TG experiments at *a* 39, 245 and 468°C , *b* and
 470 750°C .

471 **Fig. 4** Isoconversional dependency of activation energy of dehydration (loss of layered water
 472 molecules) occurring in pristine HNTs according to the different kinetic methods

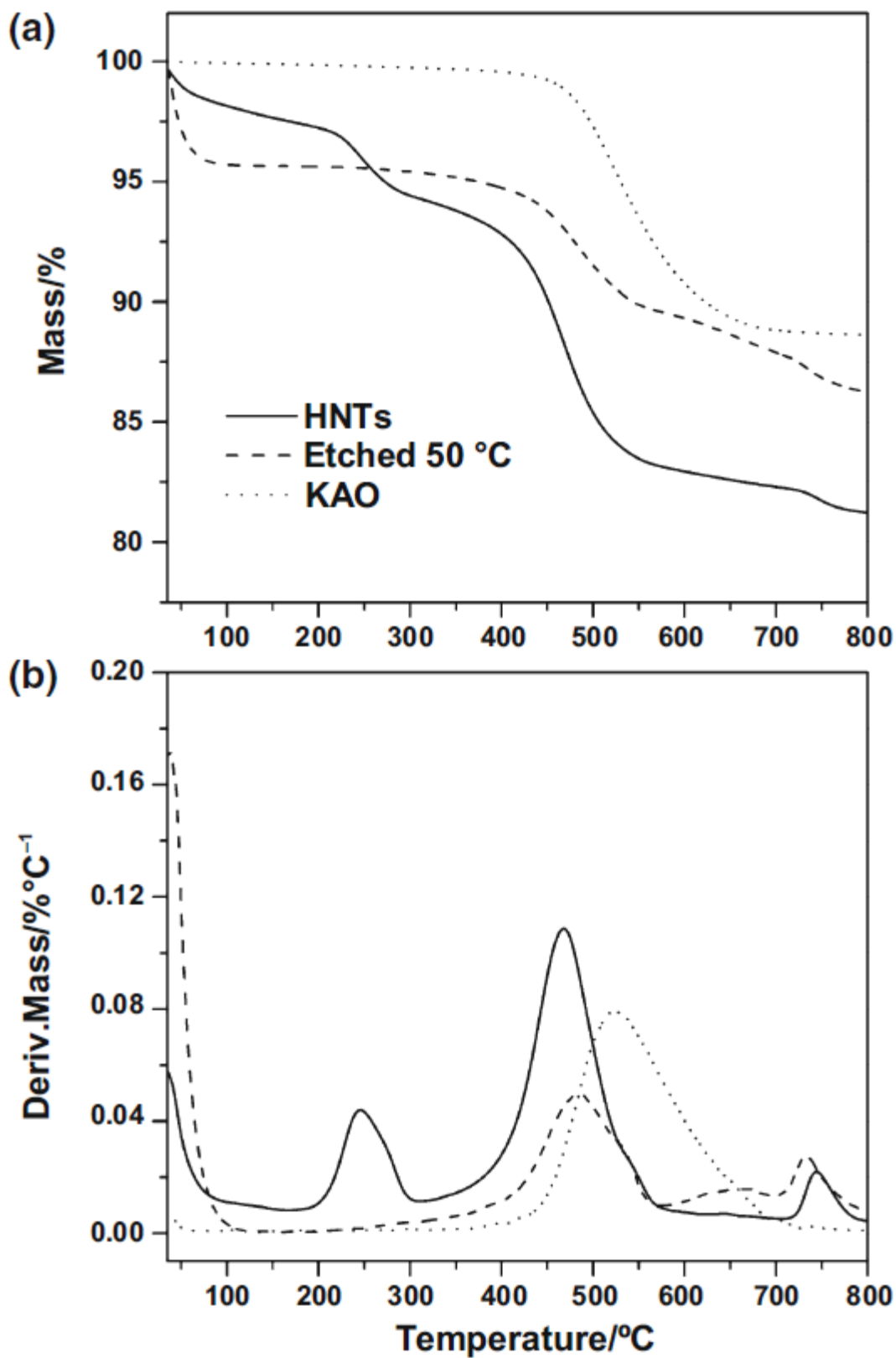
473 **Fig. 5** Isoconversional dependencies of activation energy of dehydroxylation (condensation of water
 474 due to dehydroxylation of hydroxyl groups of alumina inner sheets) according to the different
 475 kinetic methods for *a* HNTs, *b* etched HNTs, *c* KAO.

476 FIGURES



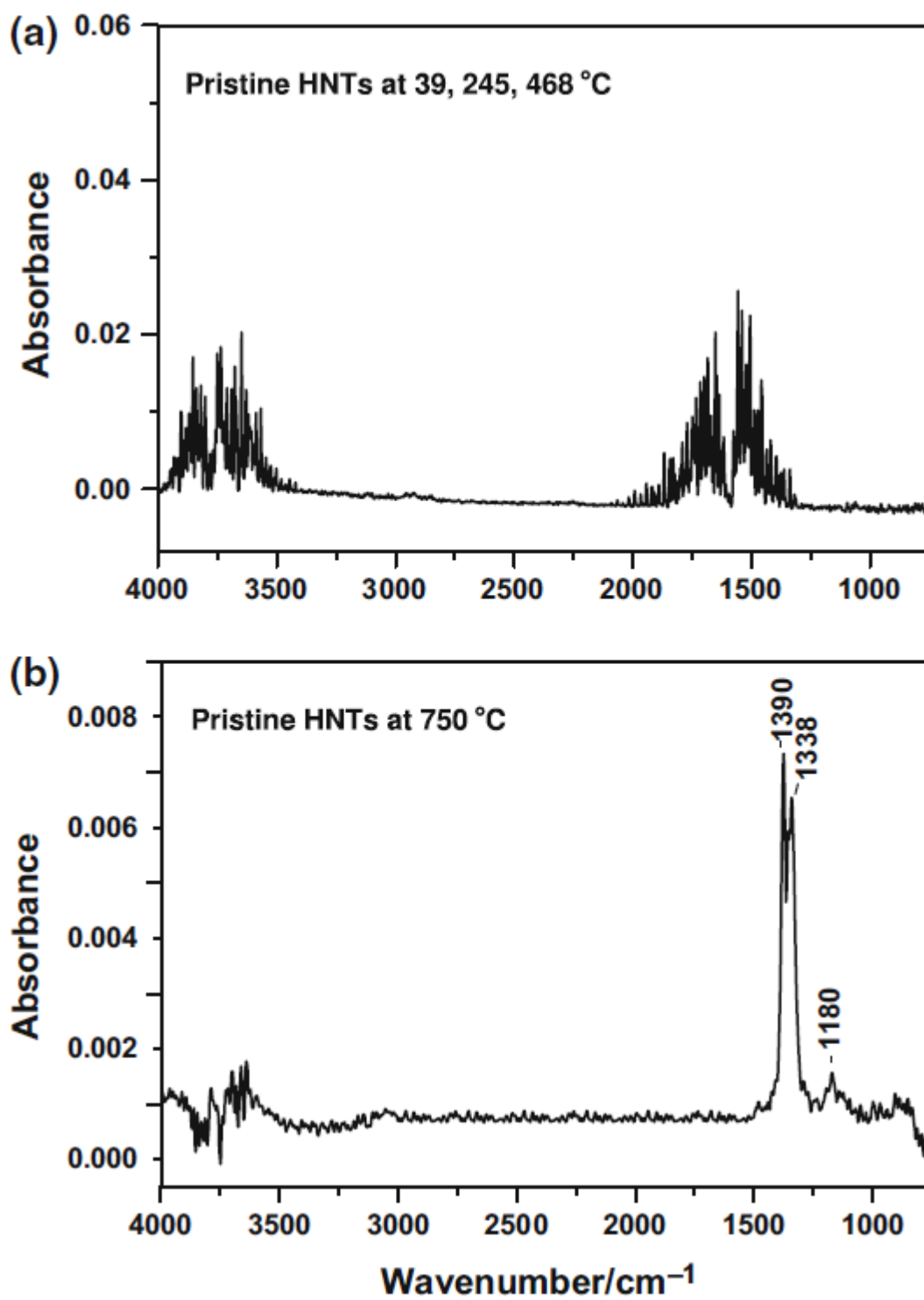
477

478 Figure 1



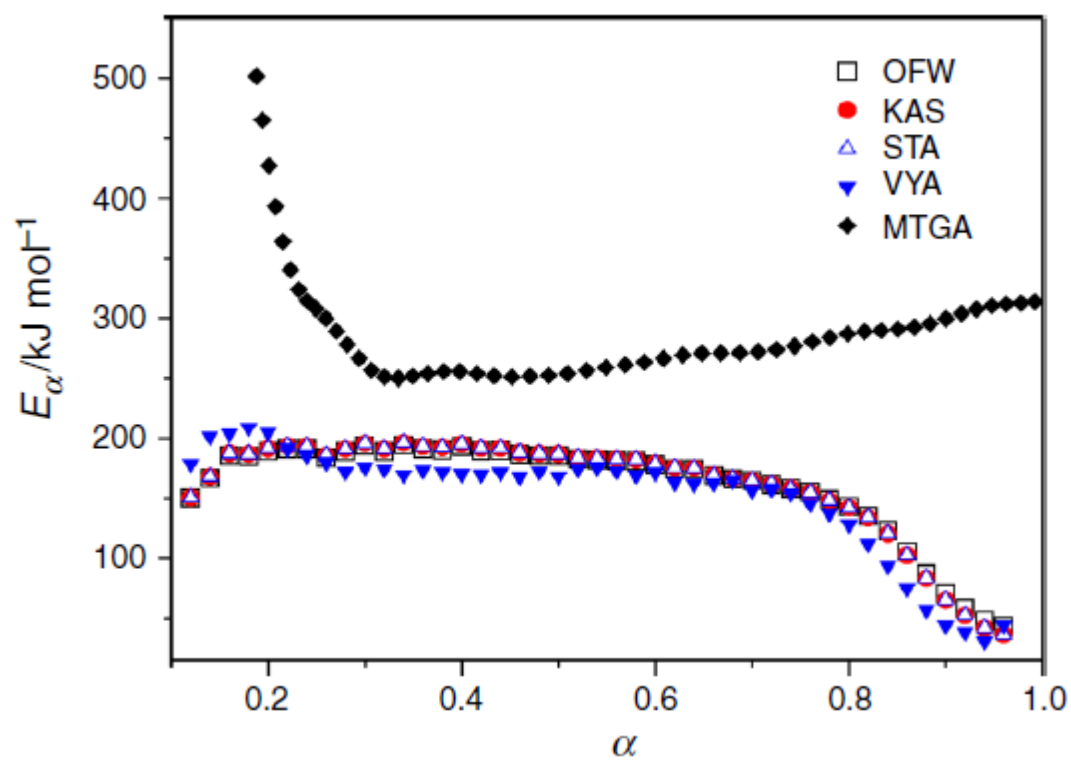
479

480 Figure 2



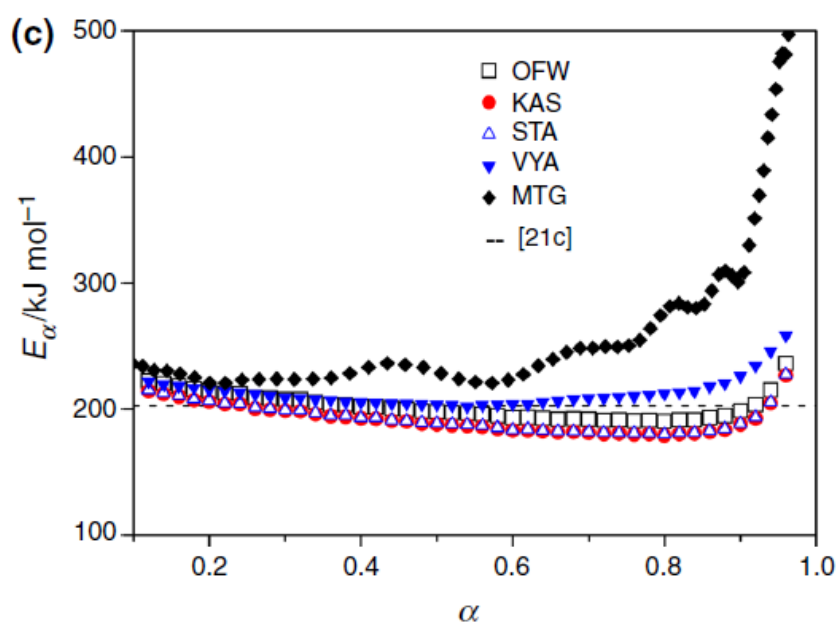
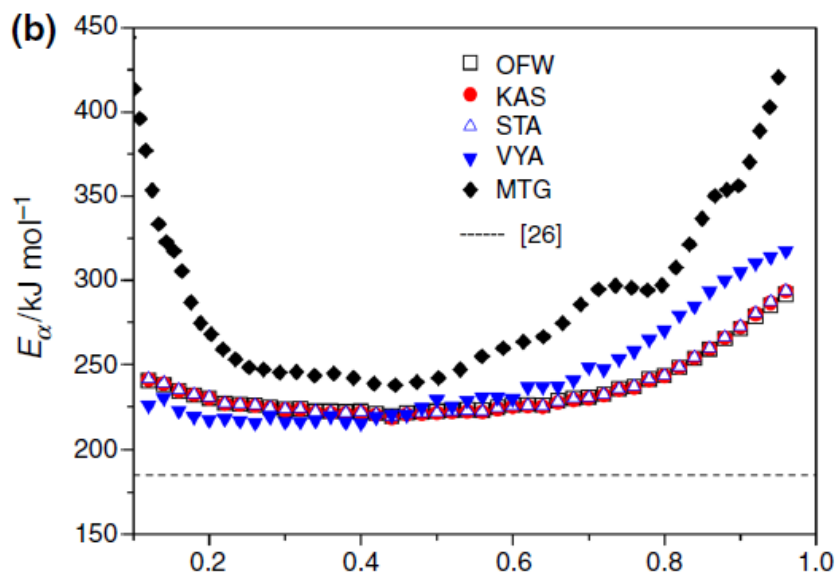
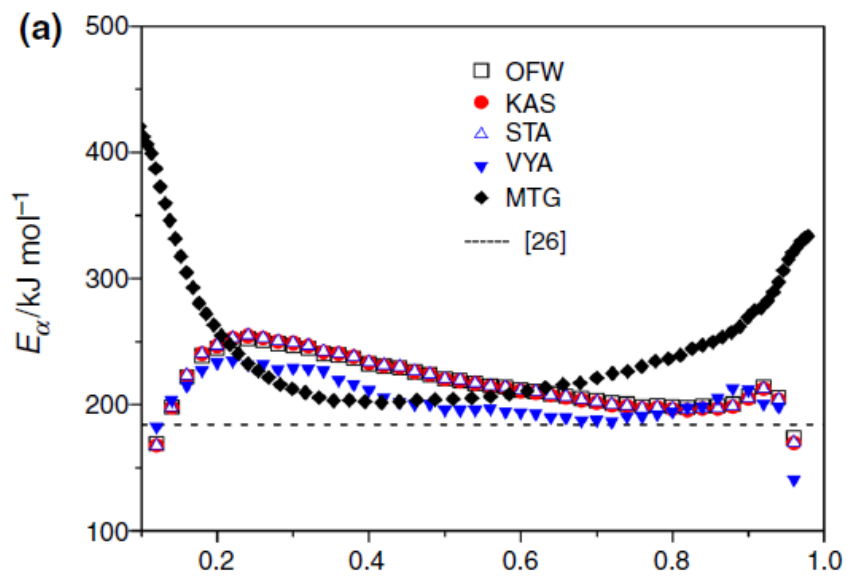
481

482 Figure 3



483

484 Figure 4



486 Figure 5

487